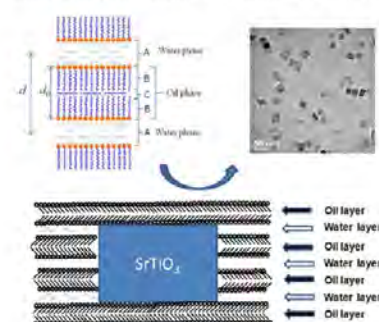


SrTiO₃ Nanocuboids from a Lamellar MicroemulsionLinhua Hu,^{*,†,‡} Chuandao Wang,[‡] Sungsik Lee,[§] Randall E. Winans,[§] Laurence D. Marks,^{*,‡} and Kenneth R. Poeppelmeier^{*,†,||}[†]Department of Chemistry and [‡]Department of Materials Science and Engineering, Northwestern University, Evanston, Illinois 60208, United States[§]X-ray Science Division and ^{||}Chemical Sciences and Engineering Division, Argonne National Laboratory, Argonne, Illinois 60439, United States

S Supporting Information

ABSTRACT: Microemulsion science has provided a wide range of possibilities in materials fabrication. Here, we describe a novel approach to the synthesis of SrTiO₃ nanoparticles of different shapes from a microemulsion. We show that the microemulsion structure plays a critical role in the shape of the nanoparticles, with diffusion-limited growth when normal or reverse micelles are present to nanocuboids with a kinetic-Wulff shape in a lamellar microemulsion leading to nanocuboids. As determined by a combination of in situ small-angle X-ray scattering (SAXS) and wide-angle X-ray scattering (WAXS) as a function of temperature and ex situ high-angle annular dark field (HAADF) imaging, the as-prepared SrTiO₃ nanocuboids grow between three layers of water (3 × 1.1 nm) and two layers of oil (2 × 2.3 nm) leading to individual crystals which are uniformly 8 nm thick with somewhat greater lengths and widths.

KEYWORDS: SrTiO₃ nanocuboids, perovskite, lamellar microemulsion, synthesis, X-ray scattering

SrTiO₃ Nanocuboids from a Lamellar Microemulsion

1. INTRODUCTION

Perovskite oxides continue to attract wide attention in a variety of different fields, for example, solid oxide fuel cells and catalysts, and various fabrication routes and strategies have been reported for nanoparticles with different sizes and shapes.^{1–15} Similarly, hydrothermal and related microemulsion techniques are now widely utilized for the fabrication of zeolites, mesoporous materials, and many nanomaterials.^{16–28} Generally, there are three major microemulsion structures in a mixture of water, oil, and surfactant: normal micelle, reverse micelle, and the lamellar liquid crystal structures. For instance, oleic acid and oleate species can form lamellar liquid crystal structures where the hydrophilic oxygen-terminated groups of the surfactants align across the water phase while the hydrophobic hydrocarbon-terminated groups align across the oil phase.^{29,30} When the mole fraction of the components change, the lamellar liquid crystal structure will convert to a normal micelle structure at low oleic acid concentration or reverse micelle structure at high oleic acid concentration. Numerous studies have exploited normal or reverse micelles for the synthesis of nanoparticles.^{25–28}

While the synthetic conditions have in many cases now become quite refined, in many examples the details of exactly why these change the nanoparticle shape are often much less clear. Here, we demonstrate that the microemulsion plays a major role in dictating the kinetics of the growth which in turn determines the overall shape. In normal or reverse micelles the

rate limiting step is diffusion in the liquid phase which, owing to the tortuosity of the structure, is slow. Atoms arriving from the solvent at the nucleation site add at the closest available site, which leads to irregular shapes. In contrast in a lamellar microemulsion the quasi-two-dimensional diffusion to the nucleation site is fast so growth is limited by conventional nucleation of new steps on the surface leading to a standard kinetic-Wulff construction. While it has been commonly assumed (without rigorous verification in most cases) that square looking perovskite nanocrystals are cubes, in this case they differ significantly in three dimensions compared to the morphology. Our findings show that the cuboid shape of as-prepared SrTiO₃ nanocrystals is a consequence of the elastic constraints of the lamellar liquid crystal structure established during the hydrothermal process.

2. EXPERIMENTAL SECTION

Materials Synthesis. For SrTiO₃ nanocuboids, 1.5 mmol of titanium butoxide (Ti(OBu)₄) was added to 52.5 mL of ethanol and 7.5 mL of oleic acid to form solution A, 1.5 mmol of strontium acetate (Sr(Ac)₂) in 15 mL of water was used to form solution B, and 1.2 g of NaOH in 6 mL of water was used to form solution C. Solutions B and C were successively added to solution A and mixed while stirring for a

Received: October 12, 2012

Revised: December 13, 2012

Published: January 8, 2013

few of minutes with a pH of 13–14, and the resultant solution was sealed in a 125 mL autoclave and then heated at 160 °C for 8 h.

The SrTiO₃ irregular rounded nanoparticles growth conditions were similar, changing 7.5 mL of oleic acid to 2 mL of oleic acid and 1.2 g of NaOH to 0.54 g of NaOH, to maintain the pH at 13–14. The SrTiO₃ nanorod growth conditions were similar, changing 7.5 mL of oleic acid to 15 mL of oleic acid and 1.2 g of NaOH to 2.1 g of NaOH, to maintain the pH at 13–14.

Chemicals. All chemicals were of analytical grade and were used as received without further purification. Distilled water without CO₂ was used throughout; Ti(OBu)₄ (99%), oleic acid (90%), Sr(Ac)₂ (99%), and ethanol were supplied by Alfa Aesar Company.

Electron Microscopy. The size and morphology of the nanocrystals were determined using a Hitachi H8100 and a HD2300 transmission electron microscope both at 200 kV and a high-resolution transmission electron microscope and scanning transmission electron microscope JEOL 2100F at 200 kV. For HAADF imaging, the inner and outer angles of the detector are 124 mRad and 268 mRad. Samples were prepared by placing several drops of a cyclohexane dispersion of the as-prepared materials on the surface of a carbon film supported on a copper grid.

Cryo-EM. A total of 5 μL of the solution was transferred to a freshly glow discharged 300-mesh copper grid covered with a thin layer of carbon film. The grid was then blotted and plunged into a reservoir of liquid ethane at its melting temperature (~90 K) at a speed of about 2–4 m/s. All the above was done in a Vitrobot (FEI). Then the grid was transferred to liquid nitrogen, mounted in a cold stage, and rapidly introduced into a JEOL 1230 transmission electron microscope operated at 100 kV.

Negative Staining. A total of 5 μL of the solution was transferred to a freshly glow discharged 300-mesh copper grid covered with a thin layer of carbon film. The grid was then blotted and stained with a 5 μL drop of 2% uranyl acetate aqueous solution. The stain solution was blotted after 30 s, and the grid was left to air-dry. The grids were imaged in a JEOL 1230 transmission electron microscope operated at 100 kV.

SAXS and WAXS. Synchrotron X-ray study was performed at Beamline 12ID-B of the Advanced Photon Source (APS) at the Argonne National Laboratory (ANL). The SAXS/WAXS data were simultaneously collected with two CCD detectors, Pilatus 2M and Pilatus 300K, covering a q range of $0.006 < q$ (Å⁻¹) < 2.4 , at a wavelength of 1.033 Å (12 keV). A 1.5 mm diameter capillary was loaded with about 0.1 mL of the as-prepared mixture and subsequently sealed. Then the capillary was placed into a stainless heating tube with a thermocouple. The reaction temperature was controlled by a home-built heating tube with a K-type thermocouple and a temperature controller (Lakeshore) for precision temperature control. Air scattering and parasitic scattering were determined by performing a measurement using an empty quartz capillary. The q range was calibrated using a silver behenate standard sample.

3. RESULT AND DISCUSSION

In this study, we used oleic acid as the surfactant to form different microemulsions in a mixture of ethanol, Ti(OBu)₄, Sr(Ac)₂, NaOH, and H₂O. Figure 1 shows typical TEM images of as-prepared nanoparticles, (a,b) when normal micelles are present, (c,d) when reverse micelles are present, and (e,f) when a lamellar morphology is present. A high-resolution TEM image in Figure S1 (see Supporting Information) shows well-ordered lattice fringes of 0.276 nm from the {110} planes as expected for single crystals. An X-ray diffraction pattern of the nanocuboids in Figure S2 (see Supporting Information) confirms the formation of cubic SrTiO₃ (JCPDC card No. 73-0661, space group *Pm3m*).

To verify the conditions during growth, in situ SAXS and WAXS were used to monitor the microemulsion structure and crystal growth of the SrTiO₃ from the mixture of oleic acid/ethanol/Ti(OBu)₄/Sr(Ac)₂/NaOH/H₂O. A 1.5 mm diameter

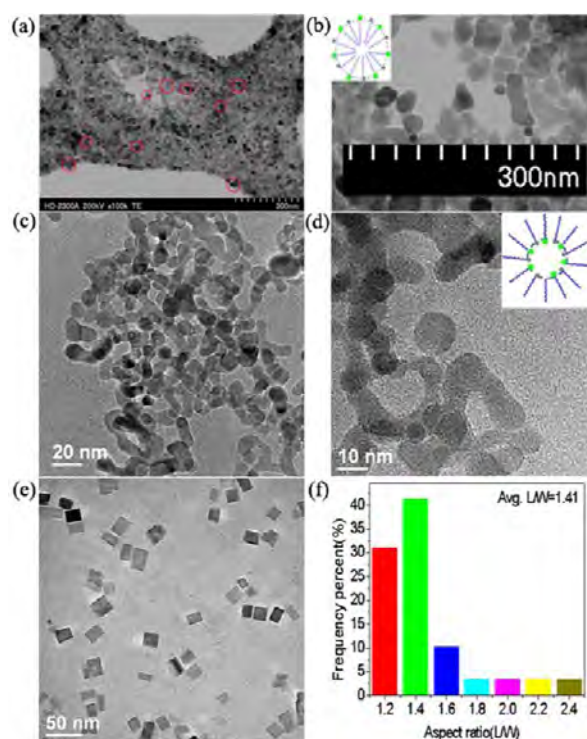


Figure 1. Different shaped SrTiO₃ nanoparticles. (a, b) TEM images of irregular rounded nanoparticles. (c, d) TEM images of nanorods. (e) TEM image of typical nanocuboids. (f) Aspect ratio (length/width: L/W) plot of SrTiO₃ nanocuboids.

capillary was loaded with about 0.1 mL of the as-prepared mixture and sealed. The capillary was placed into a stainless heating tube with a thermocouple. Figure 2a shows the SAXS profiles from 18 to 160 °C. The lamellar structure scattering vector q and the corresponding lamellar distance d at elevated temperatures are summarized in Table 1 ($d = 2\pi/q$, physics notation for the SAXS/WAXS). The spectrum obtained at 18 °C shows the typical scattering profile of a lamellar liquid crystal structure with a series of Bragg peaks. The positions of the peaks are 0.140, 0.280, and 0.420, following the q/q_1 ratios of 1:2:3 (where q_1 is the principal peak position). As shown in Figure 2b,c with more profiles at other temperatures, these peaks gradually right shift to higher wave vector with increasing temperature and a corresponding decrease of the lamellar distance. The lamellar liquid crystal structure is preserved at 160 °C.

Figure 2d shows several WAXS profiles from 18 to 105 °C. The broad peak from $q = 0.88$ to 2.4 at 18 °C is similar to those at 25, 48, 61, 73, 82, 100, and 105 °C. This broad peak centered at $q = 1.4$ is the quartz from capillary and perhaps some amorphous complex of Sr and Ti species with oleic acid. Figure 2e shows WAXS profiles from 110 to 160 °C. The profiles at 18–105 °C in Figure 2d show a significant overall reduction of the WAXS intensity for 110–160 °C which presumably originated from precipitation of SrTiO₃. SrTiO₃ is detected at 110 °C by the (110) peak of SrTiO₃ centered at 2.24 and further confirmed at higher temperatures. Therefore, SrTiO₃ starts to form between 105 and 110 °C, which is also coincident with the sharp decrease of the lamellar distance from 100 to 105 °C as shown in Figure 2c.

As a second verification of the conditions for the nanocuboids, cryo-EM techniques were used to analyze the structure

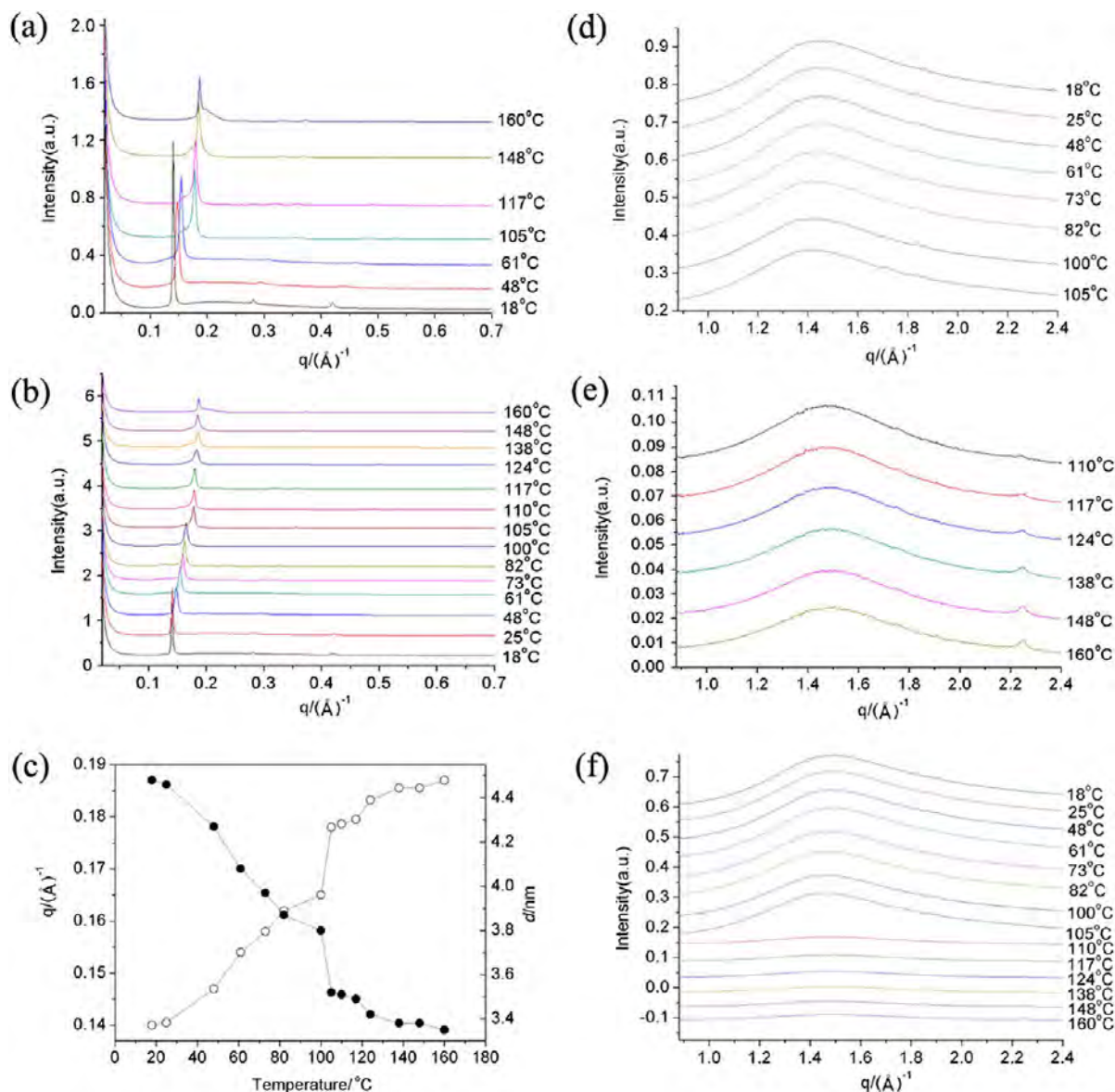


Figure 2. In situ X-ray analysis of lamellar structure. (a) SAXS profile for 7 temperatures (18–160 °C) with q from 0.08 to 0.7; (b) SAXS profile of 14 temperatures (18–160 °C) with q from 0.08 to 0.7; (c) lamellar structure scattering vector q (open circle) and lamellar distance d (filled circle) at different temperatures ($d = 2\pi/q$); (d) WAXS profile of 8 temperature points (18–105 °C) with q from 0.88 to 2.4; (e) WAXS profile at 6 temperatures (110–160 °C) with q from 0.88 to 2.4; (f) WAXS profile of 14 temperatures (18–160 °C) with q from 0.88 to 2.4.

Table 1. Scattering Vector (q) and Lamellar Distance (d) of Lamellar Structure at Different Temperatures ($d = 2\pi/q$)^a

temperature, °C	$q_1, \text{Å}^{-1}$	$q_2, \text{Å}^{-1}$	$q_3, \text{Å}^{-1}$	d_1, nm	liquid crystal structure
18	0.140	0.280	0.420	4.49	lam.
48	0.147	0.294	0.441	4.27	lam.
61	0.153	0.306	0.459	4.11	lam.
105	0.178	0.356	0.534	3.53	lam.
117	0.180	0.360		3.49	lam., STO
148	0.184	0.368		3.41	lam., STO
160	0.186	0.372		3.39	lam., STO

^aSrTiO₃ (STO) is observed above 105 °C.

of the microemulsion after the reaction had completed. As shown in Figure 3 this clearly showed the lamellar structure albeit with a different spacing since the water has been removed during the sample preparation.

Turning to a more detailed study of the sub-20 nm SrTiO₃ nanocuboids, the average aspect ratio (length/width) of these SrTiO₃ nanocuboids is ~ 1.4 (Figure 1f). To determine their true 3D morphology, based on the fact that these nanocuboids only have {100} facets, we tilted by 10–30° during HAADF operation to measure the projected edge lengths and the angles between them and then did a standard least-squares inversion to determine the true length, width, and thickness. Figures 4 and 5 show a large area HAADF image and 12 individual SrTiO₃ nanocrystals, respectively. As shown in Table 2, it is clear that these nanocrystals have one common dimension which is about 8 ± 1 nm and are different in the other two, although the volume is close to a constant. Of importance later when we discuss the growth mode, the particles as expected are covered with a self-assembled monolayer of oleic acid relatively strongly bonded to the surface. This is evidenced by the separation between the nanocuboids in Figure 4 on the grid

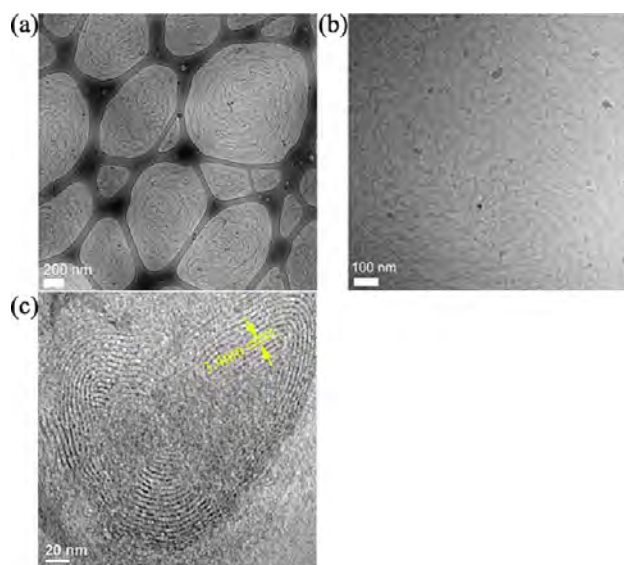


Figure 3. Direct observation of lamellar structure of oleic acid. (a,b) cyro-EM image of SrTiO₃ nanocuboids dispersed into oleic acid. (c) negative staining TEM image, showing the average 3.4 nm thickness of the double layer of oleic acid without water.

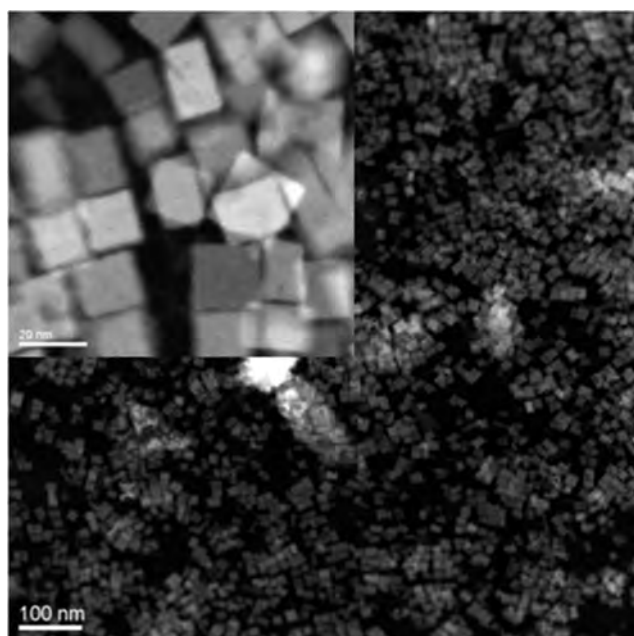


Figure 4. HAADF images of SrTiO₃ nanocuboids at different magnifications.

which is consistent with a single layer on every {001} surface with attractive hydrophobic interactions between the hydrocarbon terminations.

To understand the results, we need to analyze two coupled but different questions: what are the chemical reactions taking place during the formation of the SrTiO₃? and how does the microemulsion structure couple to the kinetics of growth?

First, we will discuss the reactions. Although different formation pathways of perovskite nanoparticles have been proposed under hydrothermal conditions when bulk TiO₂ is the reactant, most involve dissolution of the TiO₂ to form soluble Ti species and mineralization with Sr or Ba species under strongly basic conditions.^{31–34} X-ray diffraction studies

as a function of different reaction time have confirmed the gradual dissolution of TiO₂ with the nucleation and growth of SrTiO₃.³²

In our case, we use the metal alkoxide Ti(OBu)₄ as the precursor for the Ti species. Briefly, Ti(OBu)₄ is first added into oleic acid and pure ethanol to form starting solution A. The hydrolysis of Ti(OBu)₄ is limited without water. Aqueous solution B containing the Sr precursor is then added to solution A, leading to the coordination of Sr²⁺ with oleic acid at the oil–water interface (p*K*_s, equilibrium constant of Sr/oleic acid in water is about 4.95)^{35,36} with the simultaneous generation of amorphous gel from the hydrolysis of Ti(OBu)₄. Next, NaOH in water, solution C, is added into the above mixture raising the pH to 13–14 where the added base can deprotonate the oleic acid to establish the lamellar structure (see Figure 2a). The WAXS shows the absence of the bulk TiO₂ at room temperature. Therefore, the amorphous gel appears to form at the oil–water interface with Sr²⁺ oleic acid complexes.

Figure S3 (Supporting Information) schematically illustrates the water layer and oil layer of the lamellar structure. For our case, the pH is about 13–14. As shown in Table 1, the lamellar distance *d* is ~4.5 nm at 18 °C, which is the sum of the oil layer and water layer. The thickness of the oil layer is ~3.4 nm, two layers of oleic acid considering a thickness of 1.7 nm per layer of oleic acid, and the measured thickness of the water layer containing Sr, Ti, water, and ethanol is 1.1 nm.

With an increase of the temperature, the lamellar distance *d* decreased to 3.4 nm at 160 °C. No boiling of the liquid mixture was observed in the sealed capillary. The decrease of the lamellar distance mostly likely results from the bending of the more elastic long chain of the oleic acid molecule and not a change in the more robust water layer. Therefore, the oil layer thickness decreases to 2.3 nm while the water layer remains at 1.1 nm at 160 °C. As shown in Figure 6, the angle between the adjacent chain from the up and down layer is about 85°. Therefore, SrTiO₃ nuclei first form at 105–110 °C within the water layer and continue to grow on heating to 160 °C until nanocuboids with an average 8 ± 1 nm thickness are formed.

Depending upon the conditions, the shape of a nanoparticle is determined by the thermodynamic lowest energy shape at constant volume, the thermodynamic Wulff construction, or by the growth kinetics which in certain cases gives a shape that is deceptively similar, known as the kinetic-Wulff construction. The thermodynamic Wulff shape is well-documented³⁷ and will not be discussed further here. For the kinetic shape, the growth can be described by a standard differential form:³⁸

$$\partial h(\hat{n}, t)/\partial t = v\left(\hat{n}, \frac{\Delta\mu(t)}{kT}\right) \quad (1)$$

where $h(\hat{n}, t)$ is the length from some arbitrary origin to a facet whose normal is given by \hat{n} , t is time, $\Delta\mu(t)$ is the chemical potential difference between Sr and Ti in solid SrTiO₃ and the water phase of the microemulsion as a function of time, T is the temperature, k is Boltzmann's constant, and $v(\hat{n}, (\Delta\mu(t)/kT))$ is the growth velocity for the facet. Note that the change in chemical potential implicitly depends upon the Sr and Ti concentrations in the fluid phase, which may be inhomogeneous and vary with time as species diffuse through the micelle/reverse micelle/lamellar structures. If the nucleation of a new step on a surface is slow (rate-limiting) and the concentration of reactants is homogeneous, the growth velocity can be written via a face-dependent term $w(\hat{n})$ leading to the standard Frank

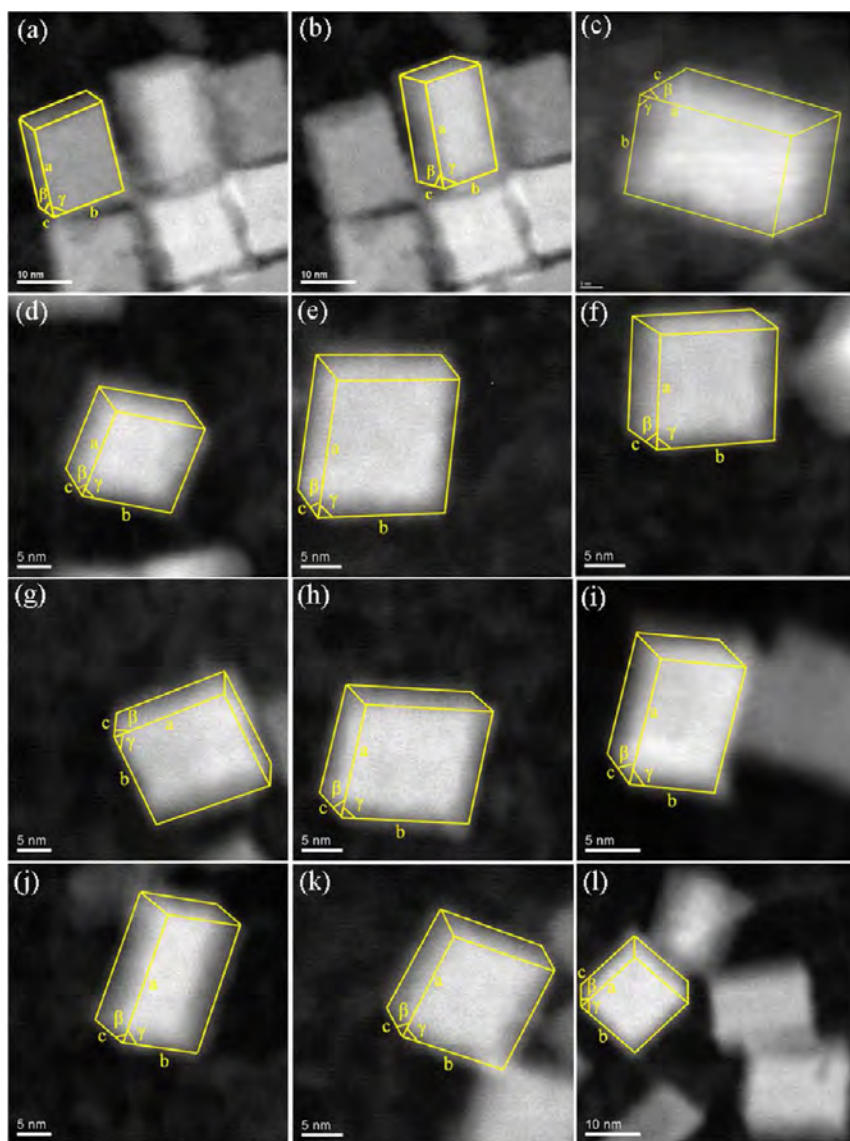


Figure 5. HAADF images of different SrTiO₃ nanocuboids. (a–l) are the nanocuboids 1–12 in Table 2.

Table 2. Results for the Three Dimensional Analysis of the SrTiO₃ Nanocuboids^a

no.	A (nm)	B (nm)	C (nm)	θ	φ	a (nm)	b (nm)	c (nm)	β	γ	error	ratio (A/B/C)
1	16.84	14.34	8.83	21.2°	21.2°	15.7	13.5	3.4	47°	82°	2.14×10^{-6}	1.90/1.62/1
2	19.83	11.56	9.17	16.6°	31.6°	19.0	10.0	5.0	65°	80°	8.60×10^{-6}	2.16/1.25/1
3	15.16	9.46	13.12	20.5°	19.3°	14.2	9.0	4.6	45°	83°	7.21×10^{-6}	1.60/1/1.39
4	14.24	14.56	8.99	23.1°	28.4°	13.1	13.1	4.6	54°	78°	2.34×10^{-6}	1.58/1.61/1
5	18.58	16.29	9.16	25.3°	22.4°	16.8	5.3	3.8	44°	79°	3.51×10^{-6}	2.02/1.77/1
6	14.79	15.61	9.07	17.6°	24.9°	14.1	14.3	4.0	57°	82°	5.11×10^{-6}	1.62/1.72/1
7	17.54	14.54	8.84	12.9°	21.3°	17.1	13.6	3.3	62°	85°	6.82×10^{-6}	1.98/1.64/1
8	14.73	16.96	8.20	20.6°	26.6°	13.8	15.4	3.9	57°	80°	6.39×10^{-6}	1.79/2.06/1
9	11.66	8.98	7.28	16.2°	26.7°	11.2	8.1	3.4	61°	82°	1.13×10^{-6}	1.60/1.23/1
10	19.88	13.04	7.77	16.5°	37.4°	19.1	10.6	4.9	70°	78°	7.48×10^{-6}	2.55/1.67/1
11	14.09	13.93	7.28	19.4°	27.9°	13.3	12.5	3.6	58°	80°	5.83×10^{-6}	1.93/1.91/1
12	13.40	13.69	8.05	17.2°	25.2°	12.8	12.5	3.6	58°	82°	2.93×10^{-6}	1.66/1.70/1

^aThe experimentally measured lengths were a , b , and c , and the projected angles are γ between a and b as well as β between a and c . A least-squares fit was performed to obtain the true length, width, and thickness of the nanocuboids A , B , and C as well as the two tilt angles θ and φ , with a priori information that the nanoparticles were cuboids. The error in the table is the root mean square (RMS) error of the fit to a , b , and c as well as the cosines of the angles.

or kinetic-Wulff construction solution for the final shape (e.g., refs 39 and 40 and references therein):

$$h(\hat{n}, t \rightarrow \infty) = \lambda w(\hat{n}) \quad (2)$$

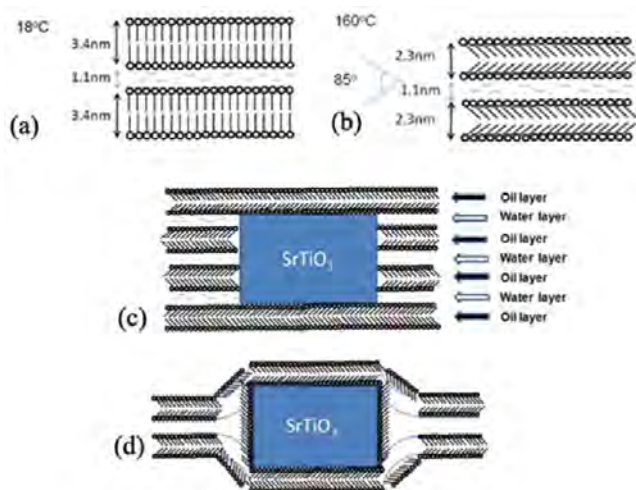


Figure 6. Schematic figure of the lamellar structure of oleic acid at different temperatures: (a) 18 °C, (b) 160 °C. (c,d) SrTiO₃ nanocuboids form three layers of water and two layers of oil, total thickness 7.9 nm, very similar to the 8 nm thickness of the synthesized SrTiO₃ nanocuboids. The reaction process is (1) coordination of Sr²⁺ with oleic acid and amorphous gel in basic condition at room temperature, (2) formation of SrTiO₃ nuclei in the water phase (water layer), and (3) growth to SrTiO₃ nanocuboids (blue color).

where λ is a constant. This is similar to the thermodynamic Wulff construction, but the external shape is now determined by the slowest growing faces. Since these tend to be those of lowest energy, for SrTiO₃ the {100} type facets will dominate the growth shape, just as they dominate the thermodynamic shape.

The kinetic-Wulff form assumes that arrival of new reactants is not rate limiting, and we argue that in the two-dimensional lamellar structure this is valid. This is not the case for the micelle or reverse-micelle cases where the oleic acid structures act as barriers to diffusion. Our interpretation is that in such a case the concentration of Sr and Ti in the liquid phase is rate limiting leading to less regular diffusion-controlled shapes as seen in many other systems.^{41,42}

Different from the {100} growth of perovskite cubes or the irregular growth in micelles/reverse micelles, SrTiO₃ nanocuboids in the lamellar liquid crystal possess a unique growth mechanism—the direction normal to the lamellar is different. The chemisorption of the oleic acid on the {100} face is relatively strong and will hinder growth, albeit it is still much smaller than the energies involved in forming SrTiO₃ so will not prevent it. More importantly, as the particles enlarge in this direction they will elastically distort the lamellar nanostructure which will lead to an increasingly large energy barrier for growth. The thickness of three water layers (3×1.1 nm) and two oil layers (2×2.3 nm) is about 7.9 nm, very similar to the average 8 nm thickness of SrTiO₃ nanocuboids. Therefore, we can infer that one water layer is broken through and SrTiO₃ forms within the adjacent two water layers and the two oil layers. The reaction scheme is summarized as (1) coordination of Sr²⁺ with oleic acid and amorphous gel in basic conditions at room temperature, (2) formation of SrTiO₃ nuclei in the water phase (water layer) at 105–110 °C, and (3) growth to SrTiO₃ nanocuboids at 160 °C. The proposed growth of SrTiO₃ nuclei to nanocuboids is summarized in Figure 6.

4. CONCLUSION

In summary, the growth of SrTiO₃ in a microemulsion is dominated by the balance between diffusion and growth kinetics. With micelles or reverse micelles diffusion dominates; in a lamellar structure sub-20 nm SrTiO₃ nanocuboids are formed. Compared to 60 nm SrTiO₃ nanocubes (20 m²/g) in our previous work,^{11,43–45} the as-prepared SrTiO₃ nanocuboids have a higher surface area of 70 m²/g and are expected to be a better support for catalysts. We believe the approach of exploiting the microemulsion structure to control the growth/diffusion kinetics can be readily extended to prepare other similar perovskite nanocrystals and to open new opportunities for design and fabrication of model catalyst with chemically well-defined and large area surfaces.

■ ASSOCIATED CONTENT

📄 Supporting Information

HREM image of a typical SrTiO₃ nanocuboid, large-angle XRD patterns of SrTiO₃ nanocuboids, and a schematic diagram of the lamellar liquid crystal structure. This material is available free of charge via the Internet at <http://pubs.acs.org>.

■ AUTHOR INFORMATION

✉ Corresponding Author

*E-mail: l-hu@northwestern.edu (L.H.), l-marks@northwestern.edu (L.D.M.), and krp@northwestern.edu (K.R.P.).

📝 Notes

The authors declare no competing financial interest.

■ ACKNOWLEDGMENTS

We acknowledge funding from Northwestern University Institute for Catalysis in Energy Processes (ICEP) on Grant DOE DE-FG02-03-ER15457. ICEP was supported by the Chemical Sciences, Geosciences, and Biosciences Division, Office of Basic Energy Sciences, Office of Science, U.S. Department of Energy. SAXS and WAXS were performed at Argonne National Laboratory. Use of the Advanced Photon Source, an Office of Science User Facility operated for the U.S. Department of Energy (DOE) Office of Science by Argonne National Laboratory, was supported by the U.S. DOE under Contract No. DE-AC02-06CH11357. The authors gratefully acknowledge the 12ID beamline staff Dr. Xiaobing Zuo for the experimental setup.

■ REFERENCES

- (1) Pena, M. A.; Fierro, J. L. G. *Chem. Rev.* **2001**, *101*, 1981–2017.
- (2) Fierro, J. L. G. In *Properties and applications of perovskite-type oxides*; Fierro, J. L. G., Tejuca, L. G., Eds.; CRC Press: 1993; pp 195–214.
- (3) O'Brien, S.; Brus, L.; Murray, C. B. *J. Am. Chem. Soc.* **2001**, *123*, 12085–12086.
- (4) Urban, J. J.; Yun, W. S.; Gu, Q.; Park, H. *J. Am. Chem. Soc.* **2002**, *124*, 1186–1187.
- (5) Mao, Y. B.; Banerjee, S.; Wong, S. S. *J. Am. Chem. Soc.* **2003**, *125*, 15718–15719.
- (6) Niederberger, M.; Pinna, N.; Polleux, J.; Antonietti, M. *J. Am. Chem. Soc.* **2004**, *126*, 9120–9126.
- (7) Niederberger, M.; Pinna, N.; Polleux, J.; Antonietti, M. *Angew. Chem., Int. Edit.* **2004**, *43*, 2270–2273.
- (8) Xu, C. Y.; Zhang, Q.; Zhang, H.; Zhen, L.; Tang, J.; Qin, L. C. *J. Am. Chem. Soc.* **2005**, *127*, 11584–11585.

- (9) Brutchey, R. L.; Yoo, E. S.; Morse, D. E. *J. Am. Chem. Soc.* **2006**, *128*, 10288–10294.
- (10) Brutchey, R. L.; Morse, D. E. *Angew. Chem., Int. Ed.* **2006**, *45*, 6564–6566.
- (11) Rabuffetti, F. A.; Kim, H. S.; Enterkin, J. A.; Wang, Y. M.; Lanier, C. H.; Marks, L. D.; Poeppelmeier, K. R.; Stair, P. C. *Chem. Mater.* **2008**, *20*, 5628–5635.
- (12) Adireddy, S.; Lin, C. K.; Cao, B. B.; Zhou, W. L.; Caruntu, G. *Chem. Mater.* **2010**, *22*, 1946–1948.
- (13) Fujinami, K.; Katagiri, K.; Kamiya, J.; Hamanaka, T.; Koumoto, K. *Nanoscale* **2010**, *2*, 2080–2083.
- (14) Urban, J. J.; Yun, W. S.; Gu, Q.; Park, H. *J. Am. Chem. Soc.* **2002**, *124*, 1186–1187.
- (15) Wang, X.; Zhuang, J.; Peng, Q.; Li, Y. D. *Nature* **2005**, *437*, 121–124.
- (16) Cundy, C. S.; Cox, P. A. *Chem. Rev.* **2003**, *103*, 663–701.
- (17) Kresge, C. T.; Leonowicz, M. E.; Roth, W. J.; Vartuli, J. C.; Beck, J. S. *Nature* **1992**, *359*, 710–712.
- (18) Zhao, D.; Feng, J. F.; Huo, Q. S.; Melosh, N.; Fredrickson, G. H.; Chmelka, B. F.; Stucky, G. D. *Science* **1998**, *279*, 548–552.
- (19) Antonietti, M.; Ozin, G. A. *Chem.—Eur. J.* **2004**, *10*, 28–41.
- (20) Peng, X. G.; Manna, L.; Yang, W. D.; Wickham, J.; Scher, E.; Kadavanich, A.; Alivisatos, A. P. *Nature* **2000**, *404*, 59–61.
- (21) Sun, Y. G.; Xia, Y. N. *Science* **2002**, *298*, 2176–2179.
- (22) Burda, C.; Chen, X. B.; Narayanan, R.; El-Sayed, M. A. *Chem. Rev.* **2005**, *105*, 1025–1102.
- (23) Jun, Y. W.; Choi, J. S.; Cheon, J. *Angew. Chem., Int. Ed.* **2006**, *45*, 3414–3439.
- (24) Tao, A. R.; Habas, S.; Yang, P. D. *Small* **2008**, *4*, 310–325.
- (25) Ge, J. P.; Chen, W.; Liu, L. P.; Li, Y. D. *Chem.—Eur. J.* **2006**, *12*, 6552–6558.
- (26) Zhao, X. J.; Bagwe, R. P.; Tan, W. H. *Adv. Mater.* **2004**, *16*, 173–176.
- (27) Ganguli, A. K.; Ahmad, T.; Vaidya, S.; Ahmed, J. *Pure Appl. Chem.* **2008**, *80*, 2451–2477.
- (28) Moulik, S. P.; Rakshit, A. K.; Capek, I. Microemulsions as templates for nanomaterials In *Microemulsions: background, new concepts, applications, perspectives*; Stubenrauch, C., Ed.; Wiley-Blackwell: 2009; pp 180–210.
- (29) Winsor, P. A. *Liquid Cryst. Plast. Cryst.* **1974**, *1*, 199–287.
- (30) Fu, Q. H.; Friberg, S. E.; Zhang, Z. Q.; Aikens, P. A. *J. Dispersion Sci. Technol.* **2000**, *21*, 1007–1021.
- (31) Eckert, J. O.; HungHouston, C. C.; Gersten, B. L.; Lencka, M. M.; Riman, R. E. *J. Am. Ceram. Soc.* **1996**, *79*, 2929–2939.
- (32) Zhang, S. C.; Liu, J. X.; Han, Y. X.; Chen, B. C.; Li, X. G. *Mater. Sci. Eng., B* **2004**, *110*, 11–17.
- (33) Knauss, K. G.; Dibley, M. J.; Bourcier, W. L.; Shaw, H. F. *Appl. Geochem.* **2001**, *16*, 1115–1128.
- (34) Tsumura, T.; Matsuoka, K.; Toyoda, M. *J. Mater. Sci. Technol.* **2010**, *26*, 33–38.
- (35) Haynes, W. M. *Handbook of Chemistry and Physics*; CRC Press: 2009.
- (36) Topallar, H.; Bayrak, Y.; Iscan, M. *Turk. J. Chem.* **1997**, *21*, 195–199.
- (37) Wulff, G. Z. *Kristallogr. Mineral.* **1901**, *34*, 449–530.
- (38) Esin, V. O.; Tarabaev, L. P.; Porozkov, V. N.; Vdovina, L. A. *J. Cryst. Growth* **1984**, *66*, 459–464.
- (39) Frank, F. C. In *Growth and perfection of crystals*; Doremus, R. H., Roberts, B. W., Tumbull, D., Eds.; John Wiley & Sons: New York, 1958; pp 3–10.
- (40) Sekerka, R. F. *Cryst. Res. Technol.* **2005**, *40*, 291–306.
- (41) Pileni, M. P. *Nat. Mater.* **2003**, *2*, 145–150.
- (42) Eastoe, J.; Hollamby, M. J.; Hudson, L. *Adv. Colloid Interface Sci.* **2006**, *128*, 5–15.
- (43) Christensen, S. T.; Elam, J. W.; Rabuffetti, F. A.; Ma, Q.; Weigand, S. J.; Lee, B.; Seifert, S.; Stair, P. C.; Poeppelmeier, K. R.; Hersam, M. C.; Bedzyk, M. J. *Small* **2009**, *5*, 750–757.
- (44) Enterkin, J. A.; Poeppelmeier, K. R.; Marks, L. D. *Nano Lett.* **2011**, *11*, 993–997.
- (45) Enterkin, J. A.; Setthapun, W.; Elam, J. W.; Christensen, S. T.; Rabuffetti, F. A.; Marks, L. D.; Stair, P. C.; Poeppelmeier, K. R.; Marshall, C. L. *ACS Catal.* **2011**, *1*, 629–635.